Novel Solid-State Sodium-Ion Battery with Wide Band Gap $NaTi_2(PO_4)_3$ Nanocrystal Electrolyte

Dai, Hanqing; Xu, Wenqian; Hu, Zhe; Chen, Yuanyuan ; Gu, Jing; Xie, Fengxian; Wei, Wei; Guo, Ruiqian; Zhang, Guoqi

DOI
10.1021/acsomega.1c00664

Publication date
2021

Document Version
Final published version

Published in
ACS Omega

Citation (APA)
Dai, H., Xu, W., Hu, Z., Chen, Y., Gu, J., Xie, F., Wei, W., Guo, R., & Zhang, G. (2021). Novel Solid-State Sodium-Ion Battery with Wide Band Gap $NaTi_2(PO_4)_3$ Nanocrystal Electrolyte. *ACS Omega*, *6*(17), 11537-11544. https://doi.org/10.1021/acsomega.1c00664

ACS OMEGA
http://pubs.acs.org/journal/acsodf
Article

Novel Solid-State Sodium-Ion Battery with Wide Band Gap $NaTi_2(PO_4)_3$ Nanocrystal Electrolyte

Hanqing Dai, Wenqian Xu, Zhe Hu, Yuanyuan Chen, Jing Gu, Fengxian Xie, Wei Wei,* Ruiqian Guo,* and Guoqi Zhang*

Cite This: *ACS Omega* 2021, 6, 11537−11544
Read Online

ACCESS | Metrics & More | Article Recommendations

ABSTRACT: $NaTi_2(PO_4)_3$ (NTP), a well-known anode material, could be used as a solid wide-band gap electrolyte. Herein, a novel solid-state sodium-ion battery (SSIB) with the thickness of electrolyte up to the millimeter level is proposed. The results of the difference in charge density investigated by the first-principles calculations imply that using the NTP nanocrystals as electrolytes to transport sodium ions is feasible. Moreover, the SSIB exhibits a high initial discharge capacity of 3250 mAh g^{-1} at the current density of 50 mA g^{-1}. As compared with other previously reported SSIBs, our results are better than those reported and suggest that the NTP nanocrystals have potential application in SSIBs as solid electrolytes.

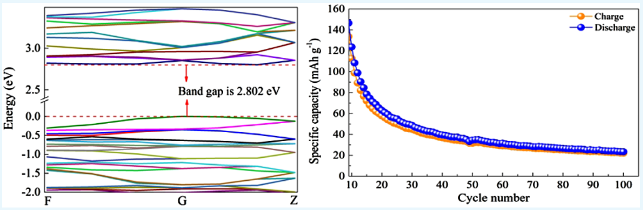

1. INTRODUCTION

Recently, the shortage of lithium resources, the booming development of electric vehicles, and intermittent energy conversions have coerced researchers into hunting for other rechargeable storage batteries with a better safety, lower costs, and higher specific energy.[1−5] Compared with lithium-ion batteries, sodium-ion batteries (SIBs) are of low cost and have plentiful resources and a high half-cell potential of sodium.[6−12] Replacing conventional flammable organic liquid electrolytes with incombustible inorganic solid electrolytes is an efficacious approach to ameliorate the safety problems of rechargeable batteries. In this regard, solid-state sodium-ion batteries (SSIBs) provide a promising possibility to the new-generation hybrid-electric vehicle due to safety, high-energy storage, high power densities, low cost, and wide availability of sodium resources.[13−16] However, several challenges should be further understood and solved in the development of solid-state electrolytes (SSEs), including a high ionic conductivity ($>10^{-2}$ S cm^{-1}), chemical stability conjugating with anode and cathode materials, appropriate electrochemical stability window, mechanical properties, etc. Solid electrolytes are provided with the function of an electrolyte and separator simultaneously for SSIBs, which determines the safety and cycling life of batteries.[17−21]

To ensure solid-state batteries operating at ambient temperature, solid electrolytes provided with superior room-temperature sodium-ion conductivity are essential.[18] Simultaneously, due to the significance of developing large-scale SSIBs, the substantial decrease in the interparticle resistance of the electrolyte is significant in the absence of a high-temperature annealing process. Nevertheless, high conductivity electrolytes suitable for the room-temperature operation of SSIBs have not yet been explored.

Over the past few years, the NASICON-type ceramic materials of $NaTi_2(PO_4)_3$ (NTP) have been considered as attractive anodes for SIBs owing to their high theoretical capacity of 132.8 mAh g^{-1}, room-temperature ionic conductivity of 10^{-4} S cm^{-1}, wide electrochemical window, and pronounced thermal stability.[22−24] However, this NTP has only one redox peak at 2.1 V in the 0−10 V range,[25−27] which means that this NTP is a potential electrolyte below the redox voltage and it can transport sodium ions because the redox reaction between electrolytes and electrodes does not occur.

As we all know, when the thickness of the electrolyte reaches the millimeter level, it could avoid the safety problems caused by dendritic growth and electrolyte penetration. Therefore, a novel SSIB with the thickness of electrolyte up to the millimeter level is proposed in this work. This novel SSIB is configured by the Na anode, NTP nanocrystal electrolytes, and the α-Fe_2O_3 cathode. Here, the NTP nanocrystal as an electrolyte was prepared at 140 °C for 3 h by a solvothermal method. Its ionic conductivity is 1.1×10^{-3} S cm^{-1} at room temperature. The electronic conductivity of the NTP was investigated by the first-principles calculations, and the results show that the valence bands are approximately horizontal, and

Received: February 9, 2021
Accepted: April 13, 2021
Published: April 22, 2021

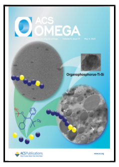

ACS Publications

https://doi.org/10.1021/acsomega.1c00664
ACS Omega 2021, 6, 11537−11544

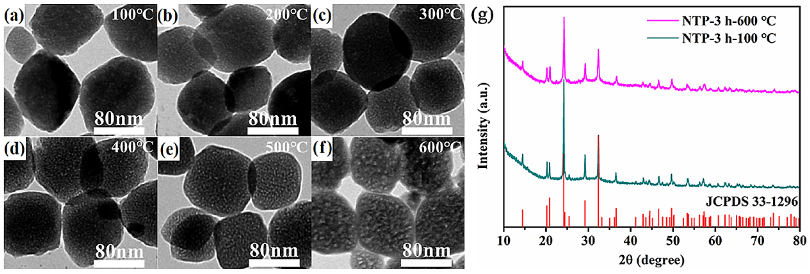

Figure 1. TEM images of the NTP nanocrystals annealed at 100−600 °C for 3 h. (a) 100 °C, (b) 200 °C, (c) 300 °C, (d) 400 °C, (e) 500 °C, (f) 600 °C, and (g) XRD patterns of the NTP nanocrystals annealed at 100 °C and 600 °C for 3 h.

the calculated band gap of the NTP is 2.802 eV. Although the wide band gap of the NTP result in poor electronic conductivity, it is beneficial for the NTP nanocrystal as an electrolyte. The results reveal that the SSIB exhibits the initial discharge capacity of 3250 mAh g^{-1} at the current density of 50 mA g^{-1}, and the mechanism of this abnormal phenomenon is explained reasonably by experiments. As compared with other previously reported SSIBs, our results are better than those reported and suggest that the NTP nanocrystals have potential application in SSIBs as solid electrolytes.

2. EXPERIMENTAL

2.1. Synthesis of Materials. *2.1.1. Synthesis of the NTP Nanocrystals.* The raw materials for synthesizing the NTP nanocrystals include sodium acetate trihydrate (2 mmol, 99.995% metals basis), titanium butoxide (2 mmol, ≥98.0 wt %), concentrated phosphoric acid (6 mL, 85 wt %), and anhydrous ethanol (24 mL). Furthermore, the above raw materials were mixed completely, and the mixture was transferred into a Teflon reactor; thereafter, the reactor was placed in an oven for the solvothermal reaction. The reactor was naturally cooled down to room temperature, and the product was washed and collected by a centrifugation method. Finally, the obtained samples were annealed at 100−600 °C for 3 h.

2.1.2. Synthesis of the Cathode Electrodes. α-Fe_2O_3 nanoceramics were successfully fabricated by the solvothermal and calcination process. The raw materials include iron chloride hexahydrate, dimethyl terephthalate, *N*,*N*-dimethylformamide, ethanol, and deionized water. First, 3 mmol iron chloride hexahydrate and 2.5 mmol dimethyl terephthalate were completely dissolved in the *N*,*N*-dimethylformamide solution (80 mL). Then, the mixture was transferred into a 100 mL Teflon autoclave and heated at 180 °C for 3 h. After the autoclave cooled at room temperature, the red product was washed with ethanol and dried at 80 °C for 24 h. Finally, the dried red powder was calcined at 380 °C for 4 h under nitrogen conditions and then annealed at 380 °C for 1 h in air to obtain α-Fe_2O_3 nanoceramics.

2.2. Structural and Morphological Characterization. The structure of the prepared materials was characterized by X-ray diffraction (XRD, Bruker D8 polycrystalline) with Cu Kα radiation (V = 30 kV, I = 25 mA, and λ = 1.5418 Å) over the 2θ range of 20°−80°. The morphology of the samples was investigated by JEM-2100 transmission electron microscopy (TEM).

2.3. Calculation Methods. NTP is a hexagonal cell, and its space group is $R\bar{3}C$ with experimental lattice parameters $a = b$ = 8.4854 Å, c = 21.7994 Å, $\alpha = \beta$ = 90°, and γ = 120°. First-principles calculations were provided by the spin-polarized GGA and LDA + U to density functional theory utilizing the CASTEP program. Using revised Perdew−Burke−Ernzerhof engenders the exchange correlation energy. The influences of different *k*-point sampling and plane-wave cutoff energies were explored in a series of test calculations. The Brillouin zone integration was performed approximately using the special *k*-point sampling scheme of Monkhorst−Pack, and a 3 × 3 × 3 *k*-point grid was used. The cutoff energy of plane wave was 600.0 eV. The maximum root-mean-square convergent tolerance was less than 2.0×10^{-5} eV/atom. The geometry optimization was stopped when all relaxation forces are less than 0.005 eV/nm. The maximum displacement error is within 0.002 nm and the maximum stress was less than 0.1 GPa.

2.4. Fabrication Process of the SSIB. The working electrode for electrochemical properties was prepared by a mixture of α-Fe_2O_3 nanoceramics, polyvinylidene fluoride (PVDF), and acetylene black (8:1:1, mass ratio). In the presence of trace 1-methyl-2-pyrrolidine (NMP), the above materials were mixed to produce a slurry. Then, it was evenly coated on aluminum foil and dried at 80 °C overnight. Finally, a coin cell of CR 2032 was assembled in an argon-filled glove box, with metallic sodium as the counter electrode and a mixture of NTP nanocrystals and PVDF (1:1, mass ratio) as an electrolyte. Because the electronic conductivity of NTP still exists, the separator is needed.

2.5. Electrochemical Measurements. The counter and reference electrodes were cylindrical stainless steel ingots. The area of all electrolytes is 0.785 cm^2. AC impedance spectroscopy of the coin cell was performed by an electrochemical workstation (CHI660E) with the frequency range from 0.0001 Hz to 100 kHz. The obtained spectra were fitted using the ZsimDemo software. The discharge−charge cycling of the coin cell was performed between 0.0 and 1.5 V on the CT-2001 LAND battery equipment (Wuhan, China). All the electrochemical measurements were investigated in a dry air atmosphere at room temperature.

3. RESULTS AND DISCUSSION

Figure 1a−f shows the TEM images of the NTP nanocrystals annealed at 100−600 °C for 3 h. With an increase in the sintering temperature, gradually the pores become larger, but the geometric size and shape of the crystals remain unchanged. After calcination at 100 °C for 3 h, the NTP is approximately a nonporous nanocrystal. However, when the calcination was performed at 600 °C for 3 h, it obviously becomes porous NTP nanocrystals because the crystal does not shrink and the pore shape changes during high-temperature sintering, which is consistent with the previous study.[28−30] This phenomenon could be explained by the diffusion and transfer of pores in the sintering of ceramic particles.[28] Figure 1g shows the XRD patterns of the NTP nanocrystals prepared at 140 °C for 3 h and annealed at 100 °C and 600 °C for 3 h. All the observed diffraction peaks perfectly match the standard diffraction peaks (JCPDS 33-1296),[22,25−27] illustrating that the NTP nanocrystals have pure phases without any impurities.

Figure 2 shows a schematic diagram of sodium ions in the transport channel of the NTP nanocrystals. From Figure 2a, it can be seen that there are many pores inside the NTP nanocrystals annealed at 600 °C for 3 h, which would lead to the inhibition of the diffusion of sodium ions and low diffusion coefficient of sodium ions (D_{Na^+}). This is consistent with the previous study.[23,24,26] However, the structure of the nonporous NTP nanocrystals is much compact, as shown in Figure 2b, and it would also be in favor of the transport of sodium ions, resulting in a high ionic conductivity and a high diffusion coefficient of the sodium ions.

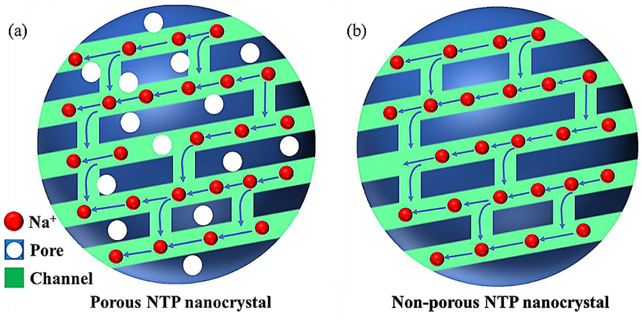

Figure 2. Sodium ions in the transport channel of the (a) porous NTP nanocrystal and (b) nonporous NTP nanocrystal.

Figure 3a illustrates the electrochemical impedance spectroscopy (EIS) of the NTP nanocrystals annealed at 100−600 °C for 3 h. The thickness and area of all of the electrolyte pellet are 0.055 ± 0.001 cm and 0.785 cm^2, respectively. An intercept implies the ohmic resistance (R_s) in the Z' axis, which indicates the resistance of the electrode and the electrolyte. The Warburg impedance (ω) is characterized by the inclined line of the low frequency. The semicircle of the middle frequency range represents the charge-transfer resistance (R_{ct}).[30−32] The results show that the nonporous NTP nanocrystal has a high ionic conductivity of 1.1 × 10^{-3} S cm^{-1} at 20 °C. The D_{Na^+} was calculated by the reported equations[33,34] from the sloping line of Figure 3b, and the kinetic parameters for the NTP nanocrystals are listed in Table 1. The D_{Na^+} of the porous NTP nanocrystals is lower than that of the nonporous NTP nanocrystals. Also, the results imply that the nonporous NTP nanocrystals annealed at 100 °C show a lower R_{ct} of 61.25 Ω and a higher D_{Na^+} value of 2.8326 × 10^{-10} cm^2 s^{-1}, which is following its outstanding ionic conductivity.

Table 1. EIS Parameters for the NTP Nanocrystals

annealed temperature (°C)	annealed time (h)	R_s (Ω)	R_{ct} (Ω)	σ_ω	D_{Na^+} (cm^2 s^{-1})
100	3	21.4	61.3	2.5	2.8 × 10^{-10}
200	3	26.5	108.6	12.9	1.0 × 10^{-11}
300	3	40.8	141.5	32.9	1.6 × 10^{-12}
400	3	45.8	145.7	33.0	1.6 × 10^{-12}
500	3	60.4	165.9	25.5	2.7 × 10^{-12}
600	3	64.9	320.4	106.1	1.6 × 10^{-13}

Ulteriorly, to comprehend the electronic conductivity of the NTP, the band structures and density of states (DOS) of the NTP crystal were investigated, as shown in Figure 4a,b, respectively. From Figure 4a, it is clearly seen that the valence bands are approximately horizontal. The calculated results show that the band gap of NTP is 2.802 eV, which is the same as reported in the literature.[35] This is probably too large to allow the transport of electrons at room temperature, which would clearly imply that the ionic conductivity of NTP is excellent. The DOS near the Fermi surface for the NTP can be evidently observed in Figure 4b. The value of the DOS near the Fermi surface for NTP (2 electrons eV^{-1}) is very low. It is generally known that only the electrons in the vicinity of the Fermi level can generate an electric current in the external electric field, and the wider band gap indicates a lower electronic conductivity.[36] These results are consistent with their excellent ionic conductivity, as shown in Table 1. Although the NTP possesses poor electronic conductivity, it is beneficial for the NTP nanocrystal as an electrolyte.

Simultaneously, the partial density of states (PDOS) of the NTP crystal with Na, Ti, P, and O is shown in Figure 4c−f, respectively. The angular momentum (*l*-dependent) origin of the various bands is obviously identifiable from the PDOS. The lowest energy group at around −57.0 eV has mainly Ti-s states. The second group at around −48.9 eV has significant contributions from Na-s states. The deeper subband group at around −33.3 eV originates from Ti-p states. The group at around −20.0 eV is formed by Na-p, P-s/p, and O-s states with a small contribution of Ti-p/d and O-p states. The groups from −10.0 eV up to the Fermi energy (E_F) originate from Ti-p/d, P-s/p, and O-s/p states. The groups from E_F and above

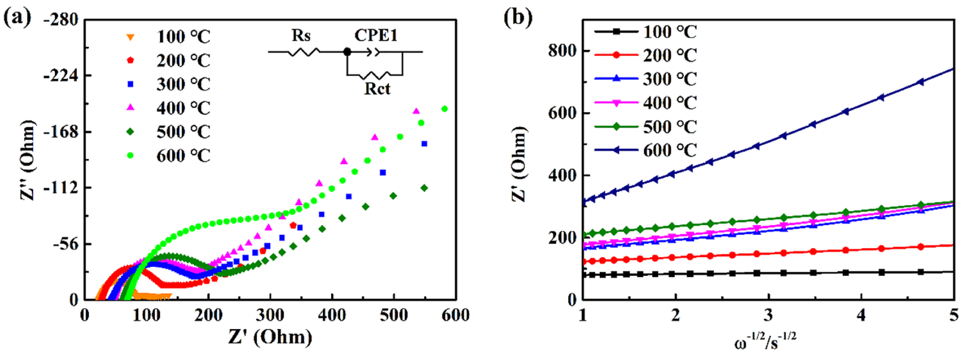

Figure 3. (a) EIS of the NTP nanocrystals annealed at 100−600 °C for 3 h (the illustration is an equivalent circuit model) and (b) the relationship plot of Z' and $\omega^{-1/2}$ at a low frequency. The area of all the testing samples is 0.785 cm^2.

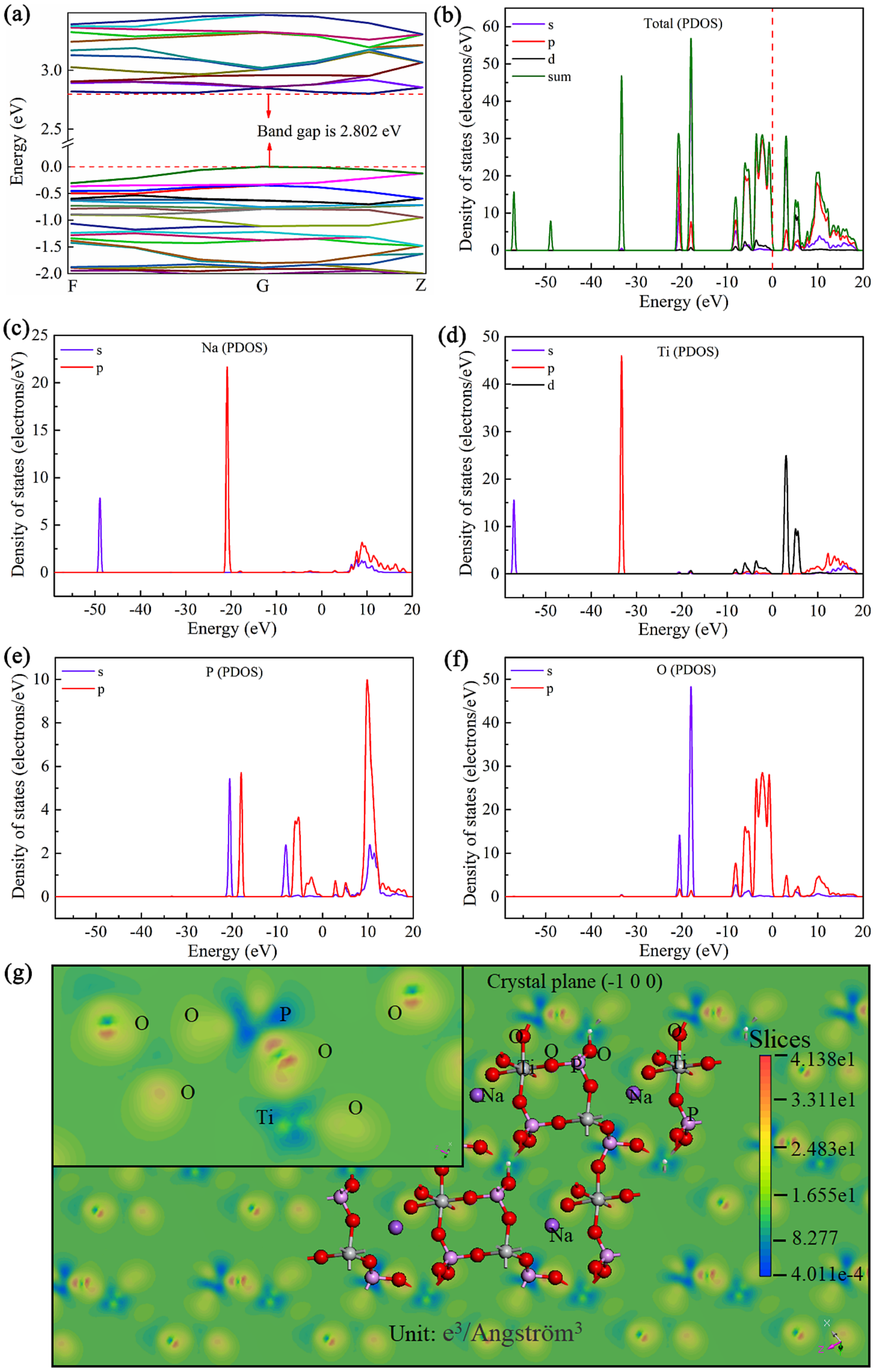

Figure 4. (a) Total band structures of the NTP crystal. (b) Total DOS of the NTP crystal. (c−f) PDOS of the NTP crystal with Na, Ti, P, and O, respectively. (g) Electric charge density difference of the crystal plane (−100) of the NTP crystal attached with a local enlargement map.

are mainly of Na-s/p, Ti-s/p, P-s/p, and O-p states. From the PDOS, we can see that there exist two strong hybridizations between Na-p and P-s at around −20.4 eV. The P-p states are hybridized with O-s states at around −17.8 eV. At about 5.0 and 10.0 eV, P-s/p orbitals are hybridized with O-p states. In addition, the difference in the charge density of the NTP with the crystal plane (−100) is shown in Figure 4g. It is obvious that the charge density around the Ti and O atoms is higher than that around the Na atom, and the Ti and O atoms maintain local charge distribution and structural stability, which means that the main contribution of the electronic conductivity of the NTP is derived from the Ti and O atoms with fixed positions. Therefore, it is feasible that the NTP nanocrystals can be used as an electrolyte to transport sodium ions. No similar results have been reported for the time being.

To prove the scientific nature of the SSIB with the millimeter-level electrolyte, the electrochemical performance of the SSIB with the NTP nanocrystal electrolyte was tested.

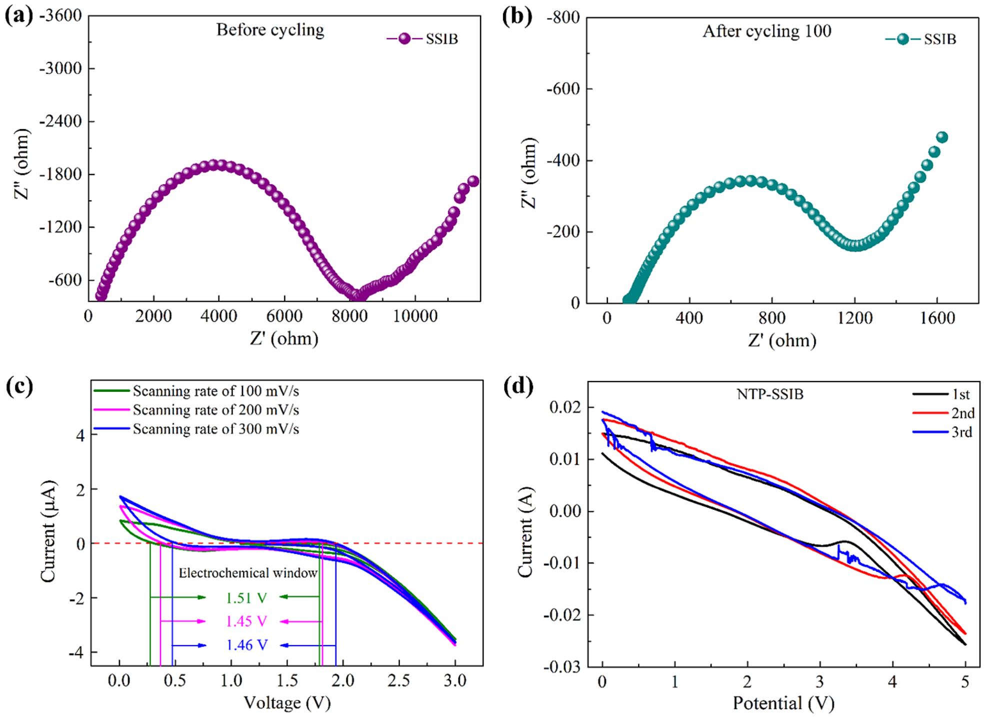

Figure 5. (a, b) EIS of the SSIB before and after cycling 100 times; (c) electrochemical stability window of NTP electrolytes on nonactive electrodes. Measurements were taken by CV on stainless steel working electrodes between 0.0 and 3.0 V at 100, 200, and 300 mV/s, respectively. The area of the nonactive electrodes is 0.785 cm^2. (d) CV curve of the SSIB.

As shown in Figure 5a,b, EIS of the SSIB illustrates that the internal resistance of the solid-state battery decreased obviously after a long-term cycling of 100 times. Figure 5c shows the electrochemical stability window of the NTP electrolytes on nonactive electrodes at different scanning rates of 100, 200, and 300 mV/s, and the results show that NTP nanocrystalline electrolytes possess an electrochemical window between 1.45 and 1.51 V. Figure 5d shows the cyclic voltammetry (CV) curve of the SSIB; the results imply the range of the oxidation−reduction potential to be of 0−1.5 and 3−4.5 V, and this SSIB could operate at the voltage range of 0−3 V with a certain capacity and a quasi-reversible process with a redox reaction (α-Fe_2O_3 + $6Na^+$ + $6e^-$ ↔ 2Fe + $3Na_2O$) between 0.0 and 5.0 V. In addition, the charge storage of the redox reaction on the surface of the transition metal oxide electrode leads to the pseudocapacitive behavior. Such a variation is caused by the unique products in the reduction of α-Fe_2O_3. Metallic Fe nanoparticles with high conductivity and electrochemically inactive Na_2O are generated after discharging the testing batteries. During the following charging process, the state of Fe and Na_2O will change gradually until the majority of Fe and Na_2O converts into α-Fe_2O_3 at the end of the oxidation reaction. Thus, during the cycles, the interface of Fe and Na_2O, as well as the conditions and electrochemical activities of the particle surface, will change slightly as the reactions progress, influencing the reactions occurring on the surface, which is exactly the pseudocapacitive reaction. These are consistent with the results of Figure 7a and the reported results.[37]

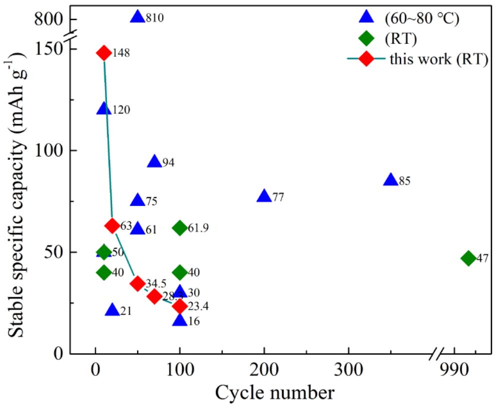

Figure 6. Electrochemical behaviors of SSIBs.[14,38−53]

Furthermore, Figure 7a shows the CV curve of the SSIB, and the results imply that the range of the oxidation−reduction potential is of 0.5−1.5 V, which is consistent with the above results. Figure 7c,d shows the cyclic stability profiles of the Na/NTP nanocrystals/α-Fe_2O_3 battery after 11 cycles. The illustration is a sheet of the electrolyte and diaphragm pressed by the force of 5 kg cm^{-2}, and the thickness of the electrolyte is about 1.6 mm (Figure 7d). It is found that the SSIB exhibits the initial discharge capacity of the first cycle to be 3250 mAh g^{-1} at the current density of 50 mA g^{-1} (Figure 7c), which far exceeds the theoretical capacity of α-Fe_2O_3 (1005 mAh g^{-1}) and NTP (132.8 mAh g^{-1}).[54,55] After 10 cycles, the discharge capacity was 148 mAh g^{-1}. After 10 cycles, the discharge capacity was 23.4 mAh g^{-1}, which is better than that reported by Deng et al. in 2019.[40] This phenomenon is mainly caused by the fact that sodium ions are embedded in the NTP electrolyte and the α-Fe_2O_3 electrode in the initial stage, and the structure of the electrolyte was obviously destroyed, which has been verified by the XRD patterns of the NTP nanocrystals before and after cycling 100 times (Figure 7b). As compared with other previously reported SSIBs (Table 2 and Figure 6),

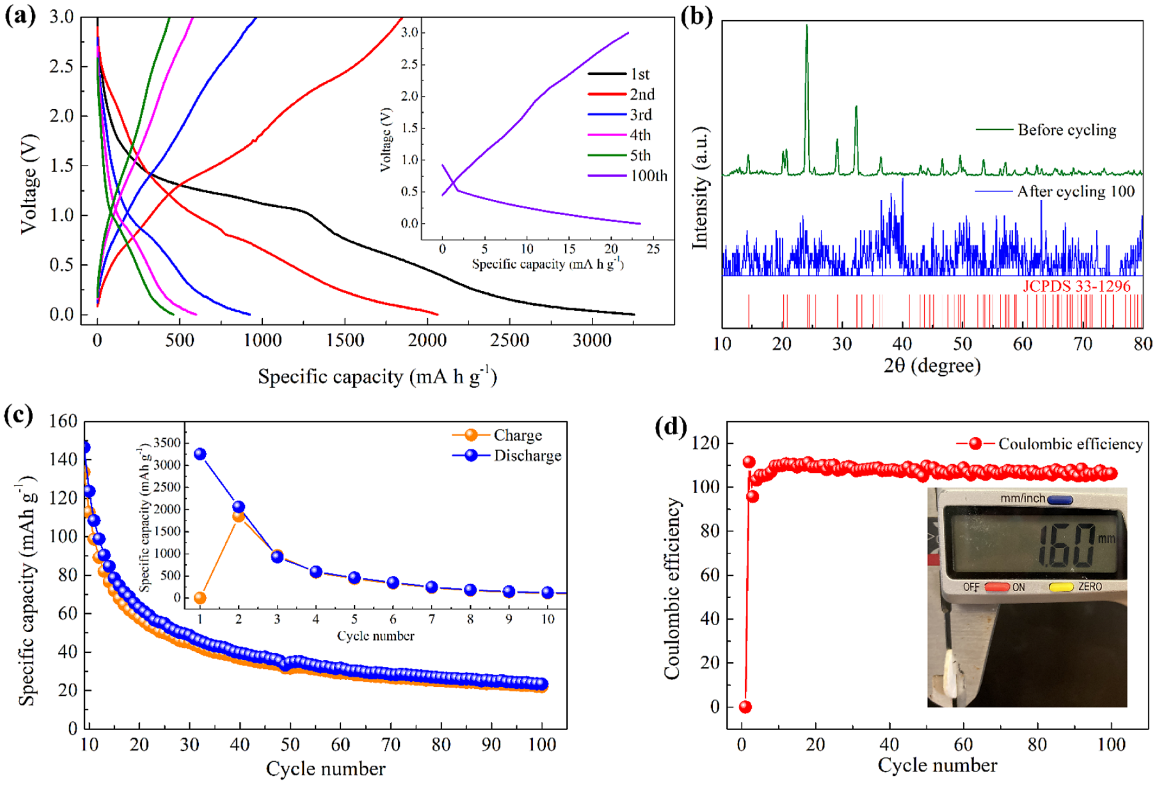

Figure 7. (a) Voltage profile of the SSIB. (b) XRD patterns of the NTP nanocrystals before and after cycling 100 times. (c, d) Cyclic stability profiles of the Na/NTP nanocrystals/α-Fe_2O_3 battery after 100 cycles. The illustration is a sheet of electrolyte and diaphragm pressed by the force of 5 kg cm^{-2}, and the area is 0.785 cm^2.

Table 2. Electrochemical Behaviors of SSIBs[14,38−53]

battery structure	thickness of electrolyte	operating temperature (°C)	stable-specific capacity (mAh g^{-1})	reference
Na_3PS_4-Na_2S-C|Na_3PS_4|Na-Sn-C		60	810 (50 mA g^{-1}, 50 cycles)	39
$NaTi_2(PO_4)_3$|H-NASICON|Na		65	94 (0.5 C, 70 cycles)	40
$Na_3V_2(PO_4)_3$|NZTO-$C_{0.02}$|Na		80	21 (0.2 C, 20 cycles)	41
Na|CPE|$Na_3V_2(PO_4)_3$		70	85 (0.5 C, 350 cycles)	42
TiS_2|$Na_3NH_2B_{12}H_{12}$/$Na_3NH_2B_{12}H_{12}$|Na		80	77 (0.1 C, 200 cycles)	43
$Na_3V_2(PO_4)_3$|CPE-ILO|Na		60	30 (2 C, 100 cycles)	44
Na-Sn|Na_3PS_4-$Na_{1.08}Sn_{1.9}PSi_{11.8}$|$TiS_2$		80	120 (4.8 mA g^{-1}, 10 cycles)	45
$Na_3V_2(PO_4)_3$|$Na_2Zn_2TeO_6$|Na		80	50 (0.2 C, 10 cycles)	46
NVP|NVPF and NVP|NVP			61 (1 C, 50 cycles)	47
δ-$Na_xV_2O_5$|SPE|Na		80	75 (60 mA g^{-1}, 50 cycles)	48
$Na_{15}Sn_4$|Na_3PS_4 glass-ceramic|$NaCrO_2$	0.5	RT	40 (64 μA cm^{-2}, 10 cycles)	49
Na_xCoO_2|NASICON|Na		RT	40 (8 μA cm^{-2}, 100 cycles)	50
Carbon|Na_2SO_4|$NaTi_2(PO_4)_3$-C		RT	61.9 (2 C, 100 cycles)	51
$NaCrO_2$|c-Na_3SbS_4|$Na_{15}Sn_4$		RT	50 (0.064 mA cm^{-2}, 10 cycles)	52
$Na_{2+2\delta}Fe_{2-\delta}(SO_4)_3$|$Na_{3.1}Sn_{0.1}P_{0.9}S_4$|$Na_2Ti_3O_7$		RT	16 (2 C, 100 cycles)	53
Na-Sn|Na_3PS_4-$Na_{11}Sn_2PSe_{12}$|TiS_2		RT	66.2 (0.1 C, 100 cycles)	54
$Na_{0.67}Ni_{0.23}Mg_{0.1}Mn_{0.67}O_2$|Na-SPE|Na		RT	47 (48 mA g^{-1}, 1000 cycles)	55
α-Fe_2O_3|$NaTi_2(PO_4)_3$|Na	1.6	RT	148 (50 mA g^{-1}, 10 cycles)	This work
			63 (50 mA g^{-1}, 20 cycles)	
			34.5 (50 mA g^{-1}, 50 cycles)	
			28.3 (50 mA g^{-1}, 70 cycles)	

the results imply that the NTP nanocrystals have potential application in the SSIBs as a solid electrolyte.

4. CONCLUSIONS

In summary, the nonporous NTP nanocrystals annealed at 100 °C show a high diffusion coefficient of sodium ions, which is in accordance with their excellent ionic conductivity. The calculated band gap of the NTP (2.802 eV) is broad, resulting in the NTP possessing poor electronic conductivity, but it is beneficial for the NTP nanocrystal as an electrolyte. It is found that the SSIB exhibits the initial discharge capacity of the first cycle to be 3250 mAh g^{-1} at the current density of 50 mA g^{-1}. As compared with other previously reported SSIBs, our results are better than those reported and suggest the NTP nanocrystals have potential application in the SSIBs as solid electrolytes.

AUTHOR INFORMATION

Corresponding Authors

Wei Wei − *College of Electronic and Optical Engineering & College of Microelectronics, Nanjing University of Posts and Telecommunications, Nanjing 210023, China*; Email: weiwei@njupt.edu.cn

Ruiqian Guo − *Institute of Future Lighting, Academy for Engineering and Technology and Institute for Electric Light Sources, Engineering Research Center of Advanced Lighting Technology, Ministry of Education, Fudan University, Shanghai 200433, China*; orcid.org/0000-0002-0498-0363; Email: rqguo@fudan.edu.cn

Guoqi Zhang − *Department of Microelectronics, Delft University of Technology, Delft 2628 CD, the Netherlands*; Email: G.Q.Zhang@tudelft.nl

Authors

Hanqing Dai − *Institute of Future Lighting, Academy for Engineering and Technology, Fudan University, Shanghai 200433, China*; orcid.org/0000-0001-5383-8702

Wenqian Xu − *College of Electronic and Optical Engineering & College of Microelectronics, Nanjing University of Posts and Telecommunications, Nanjing 210023, China*

Zhe Hu − *Institute for Electric Light Sources, Engineering Research Center of Advanced Lighting Technology, Ministry of Education, Fudan University, Shanghai 200433, China*

Yuanyuan Chen − *Institute for Electric Light Sources, Engineering Research Center of Advanced Lighting Technology, Ministry of Education, Fudan University, Shanghai 200433, China*

Jing Gu − *College of Electronic and Optical Engineering & College of Microelectronics, Nanjing University of Posts and Telecommunications, Nanjing 210023, China*

Fengxian Xie − *Institute for Electric Light Sources, Engineering Research Center of Advanced Lighting Technology, Ministry of Education, Fudan University, Shanghai 200433, China*

Complete contact information is available at: https://pubs.acs.org/10.1021/acsomega.1c00664

Notes

The authors declare no competing financial interest.

ACKNOWLEDGMENTS

Financial support from the National Natural Science Foundation of China (nos. 62075100, 62074044, 61904036, and 61675049), the Zhongshan-Fudan Joint Innovation Center, the Jihua Laboratory Projects of Guangdong Province (no. X190111UZ190), and the outstanding doctoral research promotion program of the Fudan University (no. SSH6281011/003) is gratefully acknowledged.

REFERENCES

(1) Nam, K. T.; Kim, D.-W.; Yoo, P. J.; Chiang, C.-Y.; Meethong, N.; Hammond, P. T.; Chiang, Y.-M.; Belcher, A. M. Virus-enabled synthesis and assembly of nanowires for lithium ion battery electrodes. *Science* **2006**, *312*, 885−888.

(2) Sun, X.; Si, W.; Liu, X.; Deng, J.; Xi, L.; Liu, L.; Yan, C.; Schmidt, O. G. Multifunctional Ni/NiO hybrid nanomembranes as anode materials for high-rate Li-ion batteries. *Nano Energy* **2014**, *9*, 168−175.

(3) Nitta, N.; Wu, F.; Lee, J. T.; Yushin, G. Li-ion battery materials: present and future. *Mater. Today* **2015**, *18*, 252−264.

(4) Ding, H.; Zhou, J.; Rao, A. M.; Lu, B. Cell-like-carbon-micro-spheres for robust potassium anode. *Natl. Sci. Rev.* **2020**, *8*, No. nwaa276.

(5) Shi, X.; Xu, Z.; Han, C.; Shi, R.; Wu, X.; Lu, B.; Liang, S. Highly dispersed cobalt nanoparticles embedded in nitrogen-doped graphitized carbon for fast and durable potassium storage. *Nano-Micro Lett.* **2021**, *13*, 1−12.

(6) Dai, H.; Xu, W.; Chen, Y.; Li, M.; Chen, Z.; Yang, B.; Zhang, G. Narrow band-gap cathode $Fe_3(PO_4)_2$ for sodium-ion battery with enhanced sodium storage. *Colloid Surf. A* **2020**, *591*, No. 124561.

(7) Li, Y.; Lu, Y.; Zhao, C.; Hu, Y. S.; Titirici, M. M.; Li, H.; Huang, X.; Chen, L. Recent advances of electrode materials for low-cost sodium-ion batteries towards practical application for grid energy storage. *Energy Storage Mater.* **2017**, *7*, 130−151.

(8) Dai, H.; Chen, Y.; Xu, W.; Hu, Z.; Gu, J.; Wei, X.; Zhang, G. A review of modification methods of solid electrolytes for all-solid-state sodium-ion batteries. *Energy Technol.* **2021**, *9*, No. 2000682.

(9) Sun, J.; Lee, H. W.; Pasta, M.; Yuan, H.; Zheng, G.; Sun, Y.; Li, Y.; Cui, Y. A phosphorene-graphene hybrid material as a high-capacity anode for sodium-ion batteries. *Nat. Nanotechnol.* **2015**, *10*, 980−985.

(10) Dai, H.; Xu, W.; Yu, K.; Wei, W. Concise synthesis of $NaTi_2(PO_4)_3$ nanocrystals with size and morphology control. *Chin. Chem. Lett.* **2019**, *30*, 517−520.

(11) Dai, H.; Xu, W.; Hu, Z.; Chen, Y.; Wei, X.; Yang, B.; Wei, W. Effective approaches of improving the performance of chalcogenide solid electrolytes for all-solid-state sodium-ion batteries. *Front. Energy Res.* **2020**, *8*, 1−7.

(12) Lee, D. H.; Xu, J.; Meng, Y. S. An advanced cathode for Na-ion batteries with high rate and excellent structural stability[J]. *Phys. Chem. Chem. Phys.* **2013**, *15*, 3304−3312.

(13) Banerjee, A.; Park, K. H.; Heo, J. W.; Nam, Y. J.; Moon, C. K.; Oh, S. M.; Hong, S. T.; Jung, Y. S. Na_3SbS_4: A Solution Processable Sodium Superionic Conductor for All-Solid-State Sodium-Ion Batteries. *Angew. Chem., Int. Ed.* **2016**, *55*, 9634−9638.

(14) Hou, H.; Xu, Q.; Pang, Y.; Li, L.; Wang, J.; Zhang, C.; Sun, C. Efficient Storing Energy Harvested by Triboelectric Nanogenerators Using a Safe and Durable All-Solid-State Sodium-Ion Battery. *Adv. Sci.* **2017**, *4*, No. 1700072.

(15) Yu, Z.; Shang, S. L.; Seo, J. H.; Wang, D.; Luo, X.; Huang, Q.; Chen, S.; Lu, J.; Li, X.; Liu, Z. K.; Wang, D. Exceptionally High Ionic Conductivity in $Na_3P_{0.62}As_{0.38}S_4$ with Improved Moisture Stability for Solid-State Sodium-Ion Batteries. *Adv. Mater.* **2017**, *29*, No. 1605561.

(16) Wenzel, S.; Leichtweiß, T.; Weber, D. A.; Sann, J.; Zeier, W. G.; Janek, J. Interfaces, Interfacial reactivity benchmarking of the sodium ion conductors Na_3PS_4 and sodium β-alumina for protected sodium metal anodes and sodium all-solid-state batteries. *ACS Appl. Mater. Interfaces* **2016**, *8*, 28216−28224.

(17) Delmas, C. Sodium and sodium-ion batteries: 50 years of research. *Adv. Energy Mater.* **2018**, *8*, No. 1703137.

(18) Gao, H.; Xin, S.; Xue, L.; Goodenough, J. B. Stabilizing a High-Energy-Density Rechargeable Sodium Battery with a Solid Electrolyte. *Chem* **2018**, *4*, 833−844.

(19) Carboni, M.; Manzi, J.; Armstrong, A. R.; Billaud, J.; Brutti, S.; Younesi, R. Analysis of the Solid Electrolyte Interphase on Hard Carbon Electrodes in Sodium-Ion Batteries. *ChemElectroChem* **2019**, *6*, 1745−1753.

(20) Eshetu, G. G.; Diemant, T.; Hekmatfar, M.; Grugeon, S.; Behm, R. J.; Laruelle, S.; Armand, M.; Passerini, S. Impact of the electrolyte salt anion on the solid electrolyte interphase formation in sodium ion batteries. *Nano Energy* **2019**, *55*, 327−340.

(21) Yu, X.; Manthiram, A. Sodium-Sulfur Batteries with a Polymer-Coated NASICON-type Sodium-Ion Solid Electrolyte. *Matter* **2019**, *1*, 1−13.

(22) Liang, J.; Fan, K.; Wei, Z.; Gao, X.; Song, W.; Ma, J. Porous $NaTi_2(PO_4)_3$@C nanocubes as improved anode for sodium-ion batteries. *Mater. Res. Bull.* **2018**, *99*, 343−348.

(23) Xu, Y.; Cao, W.; Yin, Y.; Sheng, J.; An, Q.; Wei, Q.; Yang, W.; Mai, L. Novel $NaTi_2(PO_4)_3$ nanowire clusters as high performance cathodes for Mg-Na hybrid-ion batteries. *Nano Energy* **2019**, *55*, 526−533.

(24) Yao, M.; Zhu, J.; Meng, W.; Li, C.; Li, C.; Wang, L.; Jiang, Z.; He, Z.; Li, Y.; Meng, W.; Zhou, H. Enhanced lithium storage performance of nanostructured $NaTi_2(PO_4)_3$ decorated by nitrogen-doped carbon. *Electrochim. Acta* **2019**, *294*, 226−232.

(25) Liu, H.; Liu, Y. 1D mesoporous $NaTi_2(PO_4)_3$/carbon nanofiber: The promising anode material for sodium-ion batteries. *Ceram. Int.* **2018**, *44*, 5813−5816.

(26) Liu, Z.; An, Y.; Pang, G.; Dong, S.; Xu, C.; Mi, C.; Zhang, X. TiN modified $NaTi_2(PO_4)_3$ as an anode material for aqueous sodium ion batteries. *Chem. Eng. J.* **2018**, *353*, 814−823.

(27) Yang, X.; Wang, K.; Wang, X.; Chang, G.; Sun, S. Carbon-coated $NaTi_2(PO_4)_3$ composite: a promising anode material for sodium-ion batteries with superior Na-storage performance. *Solid State Ionics* **2018**, *314*, 61−65.

(28) Ming, T. Y.; Fei, Z. P.; Chen, K. X.; Ping, L. A.; Yue, W. K.; Sheng, C. Y.; Zhan-Gang, L.; De-Fu, L. V. The effect of Sintering Temperature on the Structure and Properties of Corundum/mullite Ceramics. *Sci. Sintering* **2015**, *47*, 273−276.

(29) Chen, L.; Liu, J.; Guo, Z.; Wang, Y.; Wang, C.; Xia, Y. Electrochemical profile of $LiTi_2(PO_4)_3$ and $NaTi_2(PO_4)_3$ in lithium, sodium or mixed ion aqueous solutions. *J. Electrochem. Soc.* **2016**, *163*, A904−A910.

(30) Huang, Z.; Liu, L.; Yi, L.; Xiao, W.; Li, M.; Zhou, Q.; Guo, G.; Chen, X.; Shu, H.; Yang, X.; Wang, X. Facile solvothermal synthesis of $NaTi_2(PO_4)_3$/C porous plates as electrode materials for high-performance sodium ion batteries. *J. Power Sources* **2016**, *325*, 474−481.

(31) Mohamed, A. I.; Whitacre, J. F. Capacity fade of $NaTi_2(PO_4)_3$ in aqueous electrolyte solutions: relating pH increases to long term stability. *Electrochim. Acta* **2017**, *235*, 730−739.

(32) Wei, T.; Yang, G.; Wang, C. Iso-oriented $NaTi_2(PO_4)_3$ mesocrystals as anode material for high-energy and long-durability sodium-ion capacitor. *ACS Appl. Mater. Interfaces* **2017**, *9*, 31861−31870.

(33) Zhang, L. L.; Duan, S.; Yang, X. L.; Peng, G.; Liang, G.; Huang, Y. H.; Jiang, Y.; Ni, S. B.; Li, M. Reduced graphene oxide modified Li_2FeSiO_4/C composite with enhanced electrochemical performance as cathode material for lithium ion batteries. *ACS Appl. Mater. Interfaces* **2013**, *5*, 12304−12309.

(34) Qiu, H.; Yue, H.; Zhang, T.; Ju, Y.; Zhang, Y.; Guo, Z.; Wang, C.; Chen, G.; Wei, Y.; Zhang, D. Enhanced electrochemical performance of Li_2FeSiO_4/C positive electrodes for lithium-ion batteries via yttrium doping. *Electrochim. Acta* **2016**, *188*, 636−644.

(35) Voronina, N.; Jo, J. H.; Choi, J. U.; Jo, C. H.; Kim, J.; Myung, S. T. Nb-doped titanium phosphate for sodium storage: Electrochemical performance and structural insights. *J. Mater. Chem. A* **2019**, *7*, 5748−5759.

(36) Mohamed, A. I.; Sansone, N. J.; Kuei, B.; Washburn, N. R.; Whitacre, J. F. Using polypyrrole coating to improve cycling stability of $NaTi_2(PO_4)_3$ as an aqueous Na-ion anode. *J. Electrochem. Soc.* **2015**, *162*, A2201−A2207.

(37) Xiang, Y.; Yang, Z.; Wang, S.; Hossain, M. S. A.; Yu, J.; Kumar, N. A.; Yamauchi, Y. Pseudocapacitive behavior of the Fe_2O_3 anode and its contribution to high reversible capacity in lithium-ion batteries. *Nanoscale* **2018**, *10*, 18010−18018.

(38) Fan, X.; Yue, J.; Han, F.; Chen, J.; Deng, T.; Zhou, X.; Wang, C. High-performance all-solid-state Na−S battery enabled by casting−annealing technology. *ACS Nano* **2018**, *12*, 3360−3368.

(39) Zhou, W.; Li, Y.; Xin, S.; Goodenough, J. B. Rechargeable sodium all-solid-state battery. *ACS Central Sci.* **2017**, *3*, 52−57.

(40) Deng, Z.; Gu, J.; Li, Y.; Li, S.; Peng, J.; Li, X.; Han, J. Ca-doped $Na_2Zn_2TeO_6$ layered sodium conductor for all-solid-state sodium-ion batteries. *Electrochim. Acta* **2019**, *298*, 121−126.

(41) Zhang, X.; Wang, X.; Liu, S.; Tao, Z.; Chen, J. A novel PMA/PEG-based composite polymer electrolyte for all-solid-state sodium ion batteries. *Nano Res.* **2018**, *11*, 6244−6251.

(42) He, L.; Lin, H.; Li, H. F.; Filinchuk, Y.; Zhang, J.; Liu, Y.; Shao, H. $Na_3NH_2B_{12}H_{12}$ as high performance solid electrolyte for all-solid-state Na-ion batteries. *J. Power Sources* **2018**, *396*, 574−579.

(43) Chen, G.; Bai, Y.; Gao, Y.; Wang, Z.; Zhang, K.; Ni, Q.; Wu, C. Inhibition of Crystallization of Poly (ethylene oxide) by Ionic Liquid: Insight into Plasticizing Mechanism and Application for Solid-State Sodium Ion Batteries. *ACS Appl. Mater. Interfaces* **2019**, *11*, 43252−43260.

(44) Yu, Z.; Shang, S. L.; Gao, Y.; Wang, D.; Li, X.; Liu, Z. K.; Wang, D. A quaternary sodium superionic conductor-$Na_{10.8}Sn_{1.9}PS_{11.8}$. *Nano Energy* **2018**, *47*, 325−330.

(45) Li, Y.; Deng, Z.; Peng, J.; Chen, E.; Yu, Y.; Li, X.; Li, Q. A P2-Type Layered Superionic Conductor Ga-Doped $Na_2Zn_2TeO_6$ for All-Solid-State Sodium-Ion Batteries. *Chem. - Eur. J.* **2018**, *24*, 1057−1061.

(46) Sun, H.; Guo, J. Z.; Zhang, Y.; Wei, T.; Zhou, Y. X.; Zhang, L. L.; Luo, W. A high voltage all solid-state Na-ion based full cell enabled by all NASICON-structured materials. *ACS Appl. Mater. Interfaces* **2019**, *11*, 24192−24197.

(47) Zheng, Y.; Pan, Q.; Clites, M.; Byles, B. W.; Pomerantseva, E.; Li, C. Y. High-Capacity All-Solid-State Sodium Metal Battery with Hybrid Polymer Electrolytes. *Adv. Energy Mater.* **2018**, *8*, No. 1801885.

(48) Ito, Y.; Konishi, M.; Noi, K.; Deguchi, M.; Hayashi, A. Sodium thiophosphate electrolyte thin films prepared by pulsed laser deposition for bulk-type all-solid-state sodium rechargeable batteries. *J. Ceram. Soc. Jpn.* **2018**, *126*, 475−481.

(49) Kehne, P.; Guhl, C.; Ma, Q.; Tietz, F.; Alff, L.; Hausbrand, R.; Komissinskiy, P. Sc-substituted Nasicon solid electrolyte for an all-solid-state $NaxCoO_2$/Nasicon/Na sodium model battery with stable electrochemical performance. *J. Power Sources* **2019**, *409*, 86−93.

(50) Cao, X.; Yang, Y. Facile synthesis of $NaTi_2(PO_4)_3$-carbon composite through solid state method and its application in aqueous sodium ion battery. *Mater. Lett.* **2018**, *231*, 183−186.

(51) Zhang, D.; Cao, X.; Xu, D.; Wang, N.; Yu, C.; Hu, W.; Zhang, L. Synthesis of cubic Na_3SbS_4 solid electrolyte with enhanced ion transport for all-solid-state sodium-ion batteries. *Electrochim. Acta* **2018**, *259*, 100−109.

(52) Rao, R. P.; Chen, H.; Wong, L. L.; Adams, S. $Na_{3+x}M_xP_{1-x}S_4$ (M = Ge^{4+}, Ti^{4+}, Sn^{4+}) enables high rate all-solid-state Na-ion batteries $Na_{2+2\delta}Fe_{2-\delta}(SO_4)_3|Na_{3+x}M_xP_{1-x}S_4|Na_2Ti_3O_7$. *J. Mater. Chem. A* **2017**, *5*, 3377−3388.

(53) Yu, Z.; Shang, S. L.; Wang, D.; Li, Y. C.; Yennawar, H. P.; Li, G.; Wang, D. Synthesis and understanding of $Na_{11}Sn_2PSe_{12}$ with enhanced ionic conductivity for all-solid-state Na-ion battery. *Energy Storage Mater.* **2019**, *17*, 70−77.

(54) Liu, H.; Wang, G.; Park, J.; Wang, J.; Liu, H.; Zhang, C. Electrochemical performance of α-Fe_2O_3 nanorods as anode material for lithium-ion cells. *Electrochim. Acta* **2009**, *54*, 1733−1736.

(55) Bian, M.; Tian, L. Design and synthesis of three-dimensional $NaTi_2(PO_4)_3$@CNT microspheres as advanced anode materials for rechargeable sodium-ion batteries. *Ceram. Int.* **2017**, *43*, 9543−9546.